



RESEARCH ARTICLE

Responses and feedbacks of vegetation dynamics to precipitation anomaly over the semiarid area of north China: Evidences from simulations of the WRF-Noah model

Xuezhen Zhang^{1,2}  | Xinrui Liu^{1,2} | Jiazhe Chen^{1,2} | Qiuhong Tang^{1,2}  | Yilong Wang¹

¹Institute of Geographical Sciences and Natural Resources Research, Chinese Academy of Sciences (CAS), Beijing, China

²College of Resources and Environment, University of Chinese Academy of Sciences, Beijing, China

Correspondence

Xuezhen Zhang, Institute of Geographical Sciences and Natural Resources Research, Chinese Academy of Sciences (CAS), Beijing 100101, China.
Email: xzzhang@igsrr.ac.cn

Funding information

National Natural Science Foundation of China, Grant/Award Number: 41790424; National Key Research and Development Program of China, Grant/Award Number: 2019YFA0606600

Abstract

Knowledge of the responses and feedbacks of vegetation dynamics to interannual climate anomalies in the semiarid area of north China is lacking. This study addresses this issue through climate modelling for 1991–2006 with the Weather Research and Forecast (WRF) model, into which a locally empirical vegetation dynamic (VED) scheme was implemented. The VED scheme was built on the basis of regression models of the leaf area index (LAI), green vegetation fraction (GVF), and surface albedo (ALB) with ambient temperature and humidity as independent variables. Using the update WRF model, the climate simulations were carried out with turning on and off VED, respectively. By comparing the simulations outputs with each other, we find that the interannual variability of precipitation from simulations with turning on VED is larger than that from simulations with turning off VED. The larger interannual variability of precipitation could be explained by VED feedback. Vegetation growth would be more vigorous, as a response, under the more precipitation, because which brings more available water. In turn, vigorous vegetation leads to more evapotranspiration and, hence, precipitable water; as a result, there would be more precipitation. It is reversed for the years with less precipitation. Such interactions between vegetation and precipitation could be summarized as positive feedback loops. This study suggests that the interannual precipitation variability can be enlarged by VED through positive evapotranspiration–precipitation feedback. It is therefore necessary to consider the vegetation dynamics for future downscaled regional climate predictions to pursue more reliable interannual climate variability.

KEYWORDS

climate anomaly, semiarid area of north China, vegetation dynamics

1 | INTRODUCTION

The semiarid (SA) climate regime occupies a belt-like region from northeast to southwest in north China

(Zheng *et al.*, 2013) (Figure 1). In the SA climate regime, precipitation is mainly dominated by the East Asia summer monsoon (EASM), and the annual total precipitation is 300–400 mm, approximately 64.5% of which occurs in

summer (June–August) (Gong *et al.*, 2004). Due to the high variability in the EASM, the precipitation in the SA area is prominently characterized by high variability (Chen *et al.*, 2018). This is not only a transition zone between a moist climate regime and an arid climate regime but also an ecotone ranging from woodland to semidesert as well as an agro-pastoral transition zone (Liu *et al.*, 2011; Chen *et al.*, 2018; Han *et al.*, 2018). The high variability of precipitation would therefore lead to a high probability of natural disasters and deep impacts on ecosystems and society (Yu, 2016; Hao and Yu, 2018). Therefore, it is valuable to understand the contributions of factors that potentially lead to precipitation variability to improve climate prediction skills.

As an atmospheric process, precipitation variability is usually caused by ocean and atmospheric forcing. Generally, it is extensively accepted that the interannual scale of a weak EASM leading to below-normal precipitation in north China is mostly in the year following the onset of El Niño events (e.g., Ding and Chan, 2005). Recently, it was reported that such co-occurrence relations may not be fixed but rather modulated by the phase of the Pacific decadal oscillation (PDO; Feng *et al.*, 2014; Zhang *et al.*, 2018). In addition to being modulated by ocean forcing, drought in north China may also be linked to anomalies of atmospheric circulation in mid to high latitudes, such as circumglobal teleconnection patterns and Eurasian (EU) patterns (Dai *et al.*, 2020), as well as mid-latitude Silk Road patterns and meridional displacements of the Asian westerly jet (Chen *et al.*, 2021). In addition to this internal variability, the precipitation anomaly in the study area may be also caused by external forcings, such as volcanic eruptions (e.g., Bai *et al.*, 2019; Chen *et al.*, 2020).

The strong land–air interactions in the SA area (Huang *et al.*, 2017; Santanello Jr *et al.*, 2018) may also

play important roles in the local precipitation. Green vegetation may impact the local climate by modifying the surface energy budget, sensible/latent heat flux partition, and roughness (e.g., Bonan, 2008; Forzieri *et al.*, 2020). Many studies have contributed to understanding modulations of land surface dynamics on the local climate in the SA area. These studies can be classified into two categories. One category focuses on microscale physical processes to improve model parameterization through field experiments. For instance, the relations between surface albedo and solar altitude angles as well as soil moisture (Zhang *et al.*, 2003; Zheng *et al.*, 2014; 2017), turbulent flux parameterization over bare soil surfaces (Yang *et al.*, 2008), parameterization of thermal roughness length (z_{0h}) in arid and semiarid regions (Chen *et al.*, 2010), and land surface radiation and energy budget observations for semiarid sites in northwest China (Wang *et al.*, 2010) have been deeply studied. Based on the ground measurements and new parameterization, the climate models have been improved.

The second category of studies focus on the climatic effects of land cover conversions (LCCs) through climate modelling, for instance, the climatic effects of desertification in Inner Mongolia (Xue, 1996; Purevjav and Luvsan, 2004; Zhang *et al.*, 2005), grassland expansion in Hetao, Inner Mongolia (Yu *et al.*, 2013), and vegetation restoration on the Loess Plateau (Cao *et al.*, 2019; Ge *et al.*, 2020; Zhang *et al.*, 2021). These climate modelling-based studies improve our understanding of the potential climatic effects of LCCs. However, these studies have mostly focused on the effects of LCCs on climatological mean, while fewer studies have focused on the effects of LCCs on climate variability. Meanwhile, these studies focus on land cover categories conversions. Actually, in addition to categories conversions, the vegetation growth varies with climate variability and exerts significant

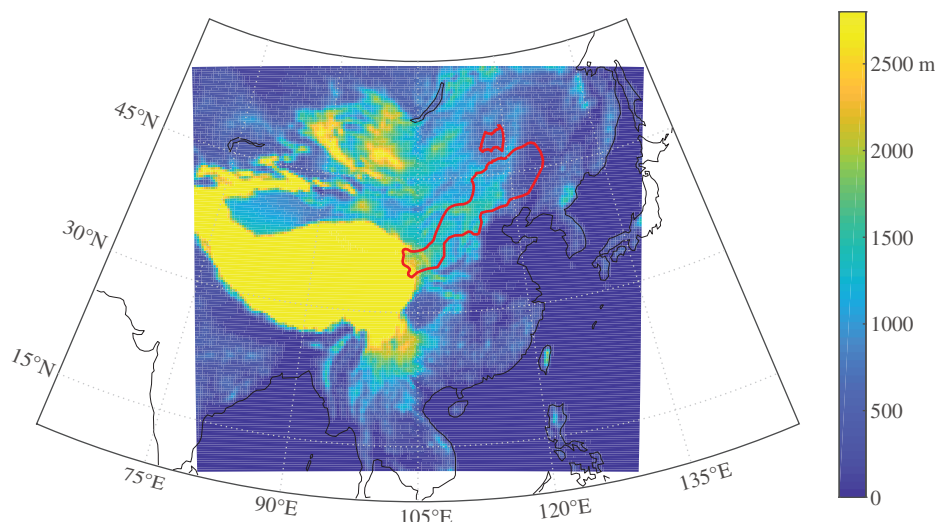


FIGURE 1 The simulation domain elevation (colourful shading; unit: meters above sea level) and study area (red polygon)

modulations on climate variability, such as in Sahel (Zeng *et al.*, 1999) and Amazon (Wang *et al.*, 2011). Since there is a semiarid climate background, the vegetation growth in the SA area is sensitive to precipitation variability (e.g., Ding *et al.*, 2020; Jiang *et al.*, 2020). In the case of more (less) precipitation, vegetation growth would usually be better (worse). To date, however, the feedbacks of such vegetation dynamics (VED) on interannual climate variability in the SA remain unclear.

In the context of such a background, this study attempted to disclose the climatic effects of the VED induced by interannual climate variability for the SA area in north China through climate modelling with the Weather Research and Forecast (WRF) model. The data and experimental design are introduced in section 2. The results for the VED model and climate modelling are presented in section 3. Section 4 compares this study with existing studies. Finally, the section 5 summarizes the whole study.

2 | DATA AND METHOD

2.1 | Data sources

This study used four sets of data. The first one is a gridded observation-based meteorology dataset, which is provided by the National Meteorology Science Data Center of China. This dataset provides monthly mean temperature and monthly total precipitation for the period from 1961 to 2018, with the spatial resolution of 0.5 by 0.5°. It was produced by spatial interpolation with the thin plate spline method on ground measurements from 2,472 meteorology stations across China (Xu *et al.*, 2009). Herein, it was used as a reference to evaluate WRF modelling.

The second one refers to sea surface temperature (SST) and the lateral boundary forcing data for the WRF modelling. It is derived from NCEP II reanalysis data, which is available from the RDA (<http://dss.ucar.edu>) in dataset number ds091.0 and has temporal interval of 6 hr and spatial grid size of 2.5 by 2.5°.

The third one is the fifth generation of the reanalysis dataset, namely, ERA5 (Hersbach *et al.*, 2020), which is provided by the European Centre for Medium-Range Weather Forecasts (ECMWF; available at <https://www.ecmwf.int/en/forecasts/datasets/reanalysis-datasets/era5>). The fourth one is the land surface parameter dataset from the Moderate Resolution Imaging Spectroradiometer (MODIS) onboard the Terra satellite and Aqua satellite (available at <https://modis.gsfc.nasa.gov/>). Both of ERA5 data and MODIS data are used to develop the new VED

scheme. More details for the two datasets are presented in Data S1, Supporting Information.

2.2 | Experimental design and data analysis

This study developed a parameterization scheme to predict vegetation dynamics (VED) induced by climate variability. Then, the VED scheme was implemented into the WRF-Noah model to replace the default scheme of user-specified fixed vegetation (Chen and Dudhia, 2001; Skamarock *et al.*, 2008). In the updated WRF-Noah model, the VED scheme would use meteorological data from WRF predictions to predict vegetation parameters including Leaf Area Index (LAI), Green Vegetation Fractions (GVF), and Albedo (ALB); in the next, these updated vegetation parameters would be used to model surface energy flux and moisture flux to atmosphere. As a consequence, interactions of climate variability and vegetation dynamic are achieved.

The VED scheme was developed through the following steps. (a) The homogeneity and heterogeneity of warm season (April–September) temperature and precipitation changes of study area during 1961–2017 were disclosed using the empirical orthogonal function (EOF) method. (b) Using results from the first step, the study area was divide into two subregions. For each subregion and each month, the highly sensitive environmental factors for vegetation growth anomalies were detected through correlations analysis between the LAI and ambient humidity and temperature. (c) Using the highly sensitive ambient factors as predictors, the regression model for LAI anomalies were calibrated. (d) The regression models for GVF and ALB anomalies with the LAI anomaly as a predictor were calibrated respectively. More details on the interannual VED parameterization scheme development and its evaluations are presented in Data S1.

Herein, the climate modelling was achieved with the WRF-Noah model into which the VED scheme was implemented. The domain of WRF modelling spans 190 grid cells in the zonal direction by 170 grid cells in the meridian direction with a centre of 35°N and 105°E and has a grid cell size of 30 by 30 km (Figure 1). The main physical parameterizations consist of the Community Atmospheric Model (CAM3) radiation scheme (Collins *et al.*, 2004), the Yonsei University planetary boundary layer scheme (Hong and Pan, 1996), the WSM3-class simple ice microphysical scheme (Hong *et al.*, 2004), and the Grell-Devenyi ensemble convection scheme (Grell and Dévényi, 2002).

Using the above configurations, we carried out two groups of experiments, which used exactly same setting but with the exception of including or excluding the VED module. One group, namely FIX experiment, excluded the VED module and used the WRF default LAI, GVF, and ALB data for the simulation periods from February 15th to October 1st for each year from 1991 to 2006. The WRF default LAI, GVF, and ALB data vary monthly but keep fixed among all the years for a given month.

The other group, namely DYN experiment, activated the VED module. The LAI, GVF, and ALB would vary with climate conditions at interannual scale. Herein, the DYN experiments kept same season with FIX experiments, that is, from February 15th to October 1st, but were carried out for 4 years with above-normal precipitation (MR years, hereafter), that is, 1993, 1996, 1998, and 2003, and 4 years with below-normal precipitation (LR years, hereafter), that is, 1997, 2001, 2002, and 2004 (section 3.3). These 8 years were selected basing on the warm season precipitation from FIX experiments and the normal referred to the mean of 1991–2006.

It is noted that we mainly focused on the differences (hereafter, Δ values) rather than the absolute values. In the DYN experiment, the monthly departures of soil temperature (T_s) and soil moisture content (θ_s) from the mean of 1991–2006 from FIX experiments, that is, ΔT_s and $\Delta \theta_s$, were calculated, and, in the next, with the VED scheme, the LAI, GVF, and ALB departures were predicted using the ΔT_s and $\Delta \theta_s$. Then, the Δ LAI, Δ GVF, and Δ ALB were added onto the WRF default monthly values used by the FIX experiments. These updated LAI,

GVF, and ALB hence were embedded in the interannual climate anomaly information and were used to calculate the surface radiation budget, evapotranspiration, and so forth to modulate the atmospheric status. Therefore, the departures of DYN simulations referring to FIX simulations represent the effects of vegetation dynamics induced by interannual climate variability.

In the next analysis section, we first compared the FIX experiments, which are used as control simulations, with ground meteorology measurements to evaluate the performance of the WRF-Noah model in the study area. Then, the departures of DYN simulations referring to FIX simulations, that is, Δ values, were analysed to disclose the response of vegetation dynamics to climate anomalies and their feedbacks on the local climate.

3 | RESULTS

3.1 | Δ LAI prediction models and their off-line performances

The prediction models for Δ LAI are crucial components of the VED scheme. The EOF analysis shows that distinct discrepancies exist in temperature and precipitation changes between the southwestern and northeastern subregions (Figure S1). Hence, in this study, Δ LAI prediction models are developed, respectively, for the southwestern and northeastern subregions. The highly sensitive ambient factors detected by correlation analysis (see section 3.2 and Table S1 for more details) are used as predictors of

TABLE 1 The LAI interannual variability prediction models for each subregion and each month

Subregion	Month	Prediction models	R^2	RMSE
Southwestern	April	$\Delta \text{LAI} = 0.0036 * \Delta T_{\text{sp1}}$	0.22*	0.0092
	May	$\Delta \text{LAI} = 0.0153 * \Delta T_{\text{sp2}}$	0.51***	0.0166
	June	$\Delta \text{LAI} = 0.0359 * \Delta T_{\text{sp3}} + 1.7211 * \Delta \theta_{\text{sp3}}$	0.59***	0.0319
	July	$\Delta \text{LAI} = 2.2321 * \Delta \theta_{\text{sp1}}$	0.30**	0.0669
	August	$\Delta \text{LAI} = 3.3634 * \Delta \theta_{\text{sp1}}$	0.66***	0.0815
	September	$\Delta \text{LAI} = 3.7045 * \Delta \theta_{\text{sp2}}$	0.35**	0.0705
Northeastern	April	$\Delta \text{LAI} = 0.0054 * \Delta T_{\text{sp1}}$	0.29**	0.0121
	May	$\Delta \text{LAI} = 0.012 * \Delta T_{\text{sp2}}$	0.64***	0.0127
	June	$\Delta \text{LAI} = 1.8214 * \Delta \theta_{\text{sp2}}$	0.44***	0.0546
	July	$\Delta \text{LAI} = 6.4206 * \Delta \theta_{\text{sp2}}$	0.54***	0.1343
	August	$\Delta \text{LAI} = 6.2832 * \Delta \theta_{\text{sp1}}$	0.46***	0.1953
	September	$\Delta \text{LAI} = 4.2204 * \Delta \theta_{\text{sp1}}$	0.40***	0.1266

Note: Δ LAI, ΔT_s , and $\Delta \theta_s$ denote, respectively, departures of leaf area index (unit: $\text{m}^2 \cdot \text{m}^{-2}$), soil temperature (unit: K), and soil moisture (unit: $\text{m}^3 \cdot \text{m}^{-3}$) of first level (0–7 cm) in the DYN experiments referring to the FIX experiments; p1, p2, and p3 denote last 1 month, last 2 months, and last 3 months, respectively. Abbreviation: RMSE, root-mean-square error.

* $p \leq 0.1$; ** $p \leq 0.05$; *** $p \leq 0.01$.

the ΔLAI . For each subregion, six monthly ΔLAI prediction models are calibrated. In total, there are 12 monthly ΔLAI prediction models (Table 1).

Among the 12 models, eight models are significant at the level of 0.01, with an explained variance of 40–66%, and three models are significant at the level of 0.05, with an explained variance of 29–35%. Only one model is significant at the level of 0.1, with an explained variance of 22%. Smaller explained variances occur in April, and larger explained variances occur in August for the southwestern subregion and in May for the northeastern subregion. The seasonal differences of explained variances could be explained by ambient limitations on the vegetation growth. In April and May, it is developing from winter to summer and it is cool. Heat resource is a limitation factor of growth (Cui, 2013; Karnieli *et al.*, 2019). Hence, significant correlation exists between LAI and T_s . Since April is the earlier growth season, grass starts sprouting and LAI is very small over the study area, while grass grows fast in May and LAI increases quickly. As a result,

the LAI in April is much lower sensitive to temperature than that in May. Since June–September, it goes into warm season and temperature is enough for vegetation growth. However, the soil moisture is not enough for vegetation growth because both of high temperature and strong solar radiation lead to high evapotranspiration (Zhang *et al.*, 2004; Song *et al.*, 2019). The significant correlations hence exist between LAI and θ_s .

These prediction models accurately reproduce the general characteristics of LAI variations for each month from 2003 to 2018 (Figure 2). For instance, the predictions reproduce the uptrend in oscillations in April, May, and June for the southwestern subregion and in July, August, and September for the northeastern subregion; they also reproduce most of the interannual variability in July, August, and September for the southwestern subregion and April, May, and June for the northeastern subregion. The predictions have a low ability to reproduce the extreme values, such as in April 2013 for the northeastern subregion and in April 2003 for the southwestern

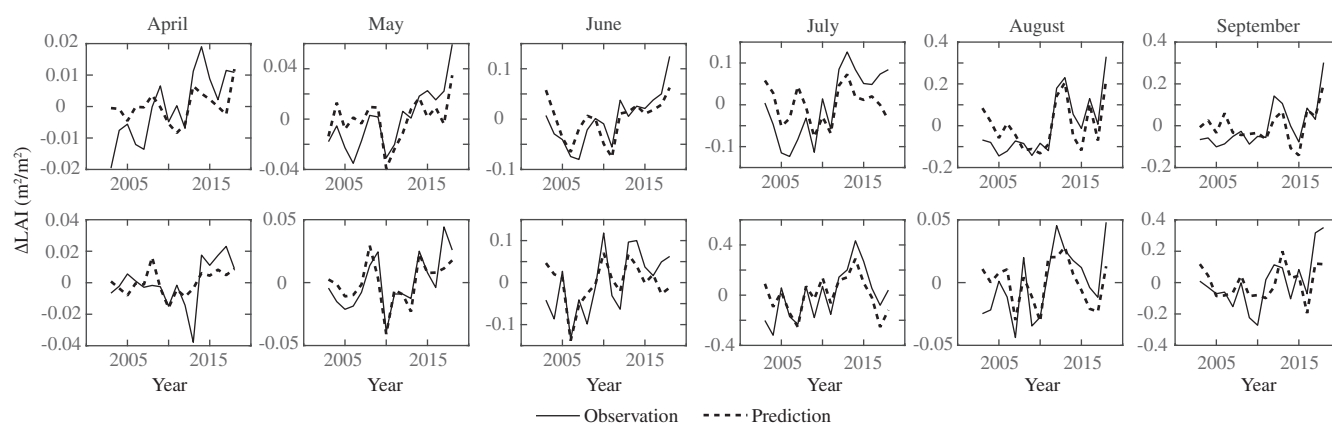


FIGURE 2 Observed and predicted ΔLAI (referring to mean of 2003–2018) for each month over southwestern subregion (top panel) and northeastern subregion (bottom panel) from 2003 to 2018

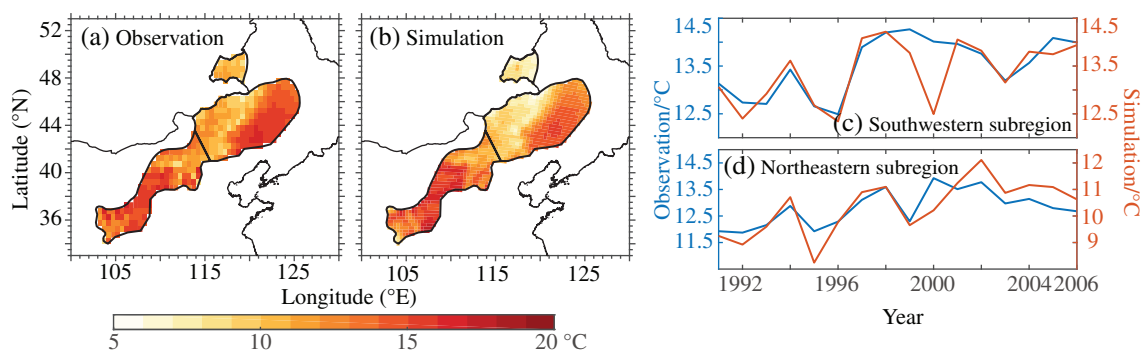


FIGURE 3 Observation (a) and WRF simulation (b) of mean April–September temperature over the period of 1991–2006 and interannual temperature variations for southwestern subregion (c) and northeastern subregion (d) from 1991 to 2006 [Colour figure can be viewed at wileyonlinelibrary.com]

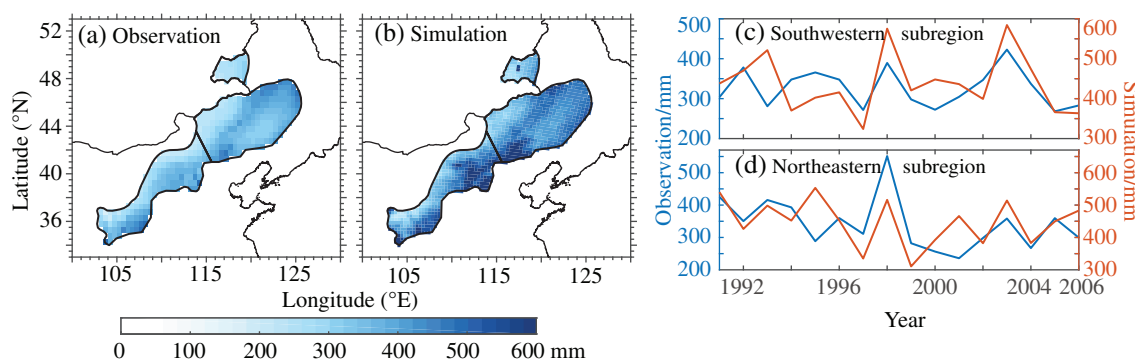


FIGURE 4 Same with Figure 3, but for total precipitation [Colour figure can be viewed at [wileyonlinelibrary.com](https://onlinelibrary.wiley.com/doi/10.1002/joc.7830)]

subregion. Actually, the lower ability of the prediction extreme is the shortage of the linear regression model.

3.2 | Evaluations of the WRF-Noah model

Figures 3 and 4 present the spatial and temporal variations of simulated and observed temperature and precipitation, respectively, for the study area. It shows that simulation captures most of the observed spatial and temporal variations. Both simulation and observation present relatively high temperatures over the southeastern partition of the northeastern subregion and middle of the southwestern subregion (Figure 3). The spatial variations from simulation and observation are highly correlated ($r = .86$, $p < .001$) with each other. For the temporal variations, the simulation could also keep approximately the same interannual variability phases as the observations, except for an abnormal cooling bias of $\sim 1.5^{\circ}\text{C}$ in 2000 for the southwestern subregion. For the northeastern subregion, the simulation is also approximately in the same phase as the observations. The cooling bias in 2000 for the northeastern subregion has been detected in many regional climate models (e.g., Ge *et al.*, 2014). The cooling bias may in part result from lateral boundary forcing data bias or physical parameterization uncertainties. It is out of the scope of this study to clarify reasons leading to a single year with bias, and we have not discussed this issue deeply in this study.

Figure 4 shows that the simulation also captures the general spatial variability of precipitation with $r = .73$ ($p < .001$). There is more precipitation in the central partition and less precipitation along the western edge of the study area. The simulation also mostly reproduces the interannual variability in precipitation. There was more prominent precipitation in 1998 and 2003 and less precipitation in 1997. However, the simulation presents a higher mean precipitation than the observation

climatological mean by approximately 100 mm, amounting to approximately 30% of the observation mean. In comparison to temperature simulation, precipitation simulation is a much harder issue. The main challenge may be derived from microphysical parameterization and cumulus convection parameterization.

3.3 | Effects of vegetation dynamics on climate simulation

As shown in Figure 4, the interannual variability in precipitation is not exactly same with each other between the two subregions. Here, the MR and LR years were selected following the criteria that signs of precipitation anomalies referring to the mean of 1991–2006 kept same with each other between the two subregions and total precipitation anomalies of two subregions were as larger as possible. As a result, 1993, 1996, 1998, and 2003 were selected as MR years, and 1997, 2001, 2002, and 2004 were selected as LR years. For the four MR years, the ground-measured regional mean precipitation anomalies reached a maximum of $\sim 38\%$ in 1998, and for the four LR years, it reached a minimum of $\sim -16\%$ in 2001.

The month in which large abnormal precipitation occurred varied by year, and the strengths and signs of precipitation anomalies may be also different between two subregions. As a response to the precipitation anomalies, the ΔLAI , ΔGVF , and ΔALB also exhibit large variability among the months and subregions. Taking the MR years as an example, the positively larger ΔLAI in the DYN simulations referring to the FIX simulations occurs in summer for both subregions, whereas the ΔLAI in the DYN simulations is negative in spring for the southwestern subregion (Figure 5). For 2004, one of the LR years, the ΔLAI in the DYN simulations is a little positive in the southwestern subregion, whereas it was largely negative in the northeastern subregion. For 1997 and 2002, which are also LR years, there were negative

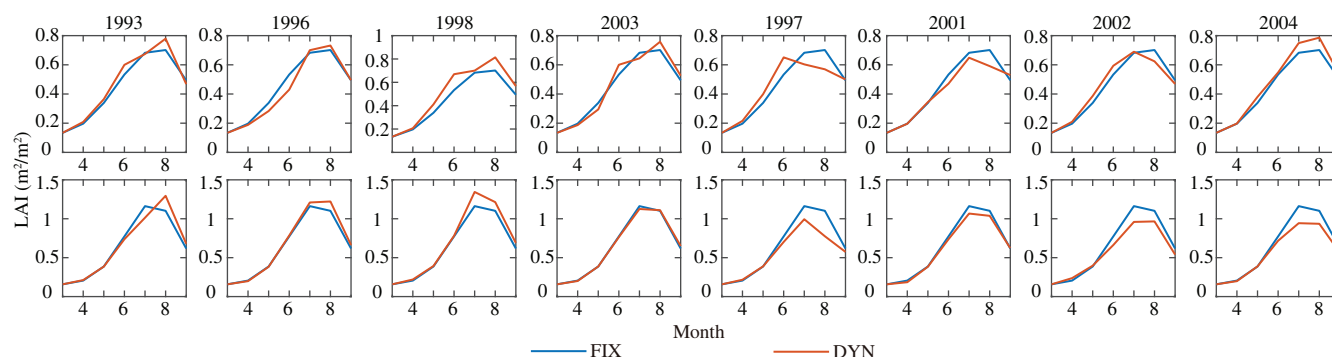


FIGURE 5 Regional mean monthly LAI from March to September for the southwestern subregion (top panel) and northeastern subregion (bottom panel) from FIX experiment and DYN experiment for more rainfall years (i.e., MR years, left four panels: 1993, 1996, 1998, and 2003) and less rainfall years (i.e., LR years, right four panels: 1997, 2001, 2002, and 2004) [Colour figure can be viewed at wileyonlinelibrary.com]

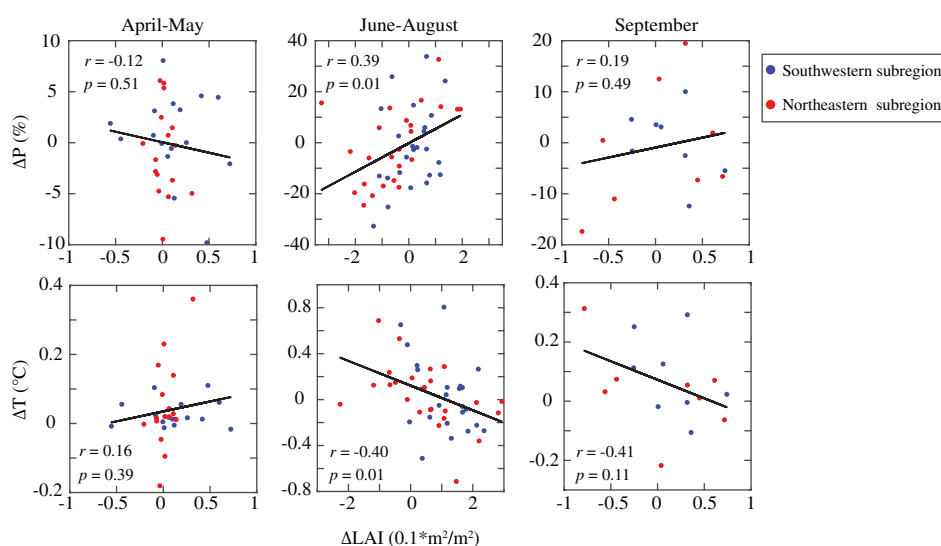


FIGURE 6 Scatter plots of regional mean ΔP and ΔT against ΔLAI in the DYN experiment referring to the FIX experiment [Colour figure can be viewed at wileyonlinelibrary.com]

ΔLAI in summer but positive ΔLAI in spring in the DYN simulations for the northeastern subregion. These large variability among the months and subregions provides many samples to study the climatic effects of vegetation dynamics.

Figure 6 shows that there is a significantly positive correlation ($r = .39$, $p < .01$) between summer ΔP in DYN simulations referring to FIX simulations and contemporaneous ΔLAI and a significantly negative correlation ($r = -.40$, $p < .01$) between the summer ΔT and ΔLAI . These correlations indicate that the most prominent effects of vegetation growth on the local climate are cooling and precipitation effects in summer. Along with the LAI increase of $0.1 \text{ m}^2/\text{m}^2$, there was an increase in precipitation of $\sim 11\%$ and a cooling of 0.1°C for the summer. It is notable that the correlation in the northeastern subregion is likely stronger than that in the southwestern subregion. For the northeastern subregion, the stronger precipitation correlation mainly occurs in the north-end

partition and central-south partition rather than over the entire subregion (Figure 7a). The domain of the strong correlation for temperature is larger than that of precipitation, but it mainly refers to the rainless-day temperature (Figure 7b) rather than rainfall-day temperature (Figure 7c).

For spring (April–May) and early autumn (September), no significant correlations could be detected (Figure 6). However, the negative correlations between the ΔLAI and ΔT in spring could actually be detected with ground measurements (e.g., *Wi et al., 2011*). Herein, the nonsignificant correlation may be explained by minor ΔLAI from the prediction models. The minor ΔLAI is partly determined by low LAI values in spring and autumn, which are the beginning and end of the growth season, respectively. The minor ΔLAI may also be caused by the low ability of the prediction models, which may only explain 20–30% and 30–40% of the LAI variations for April and September, respectively (Table 1).

FIGURE 7 Correlations between summer ΔP (a), ΔT of rainless days (b), ΔT of rainfall days (c) and ΔLAI in the DYN experiment referring to FIX experiment (black dots denote the p values of $\leq .05$)

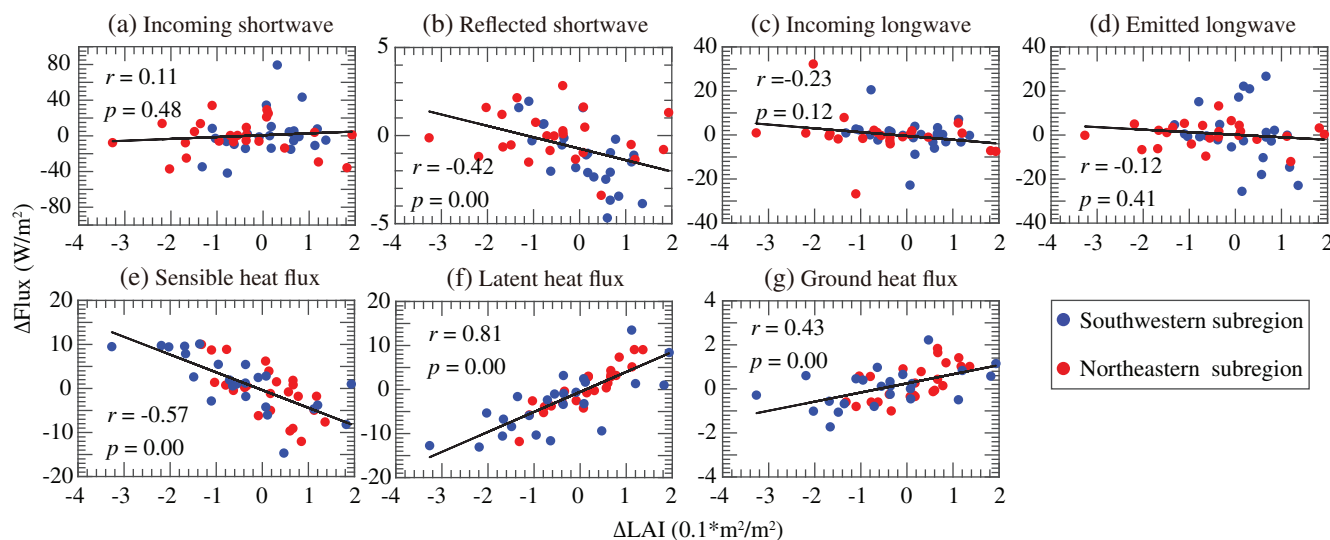
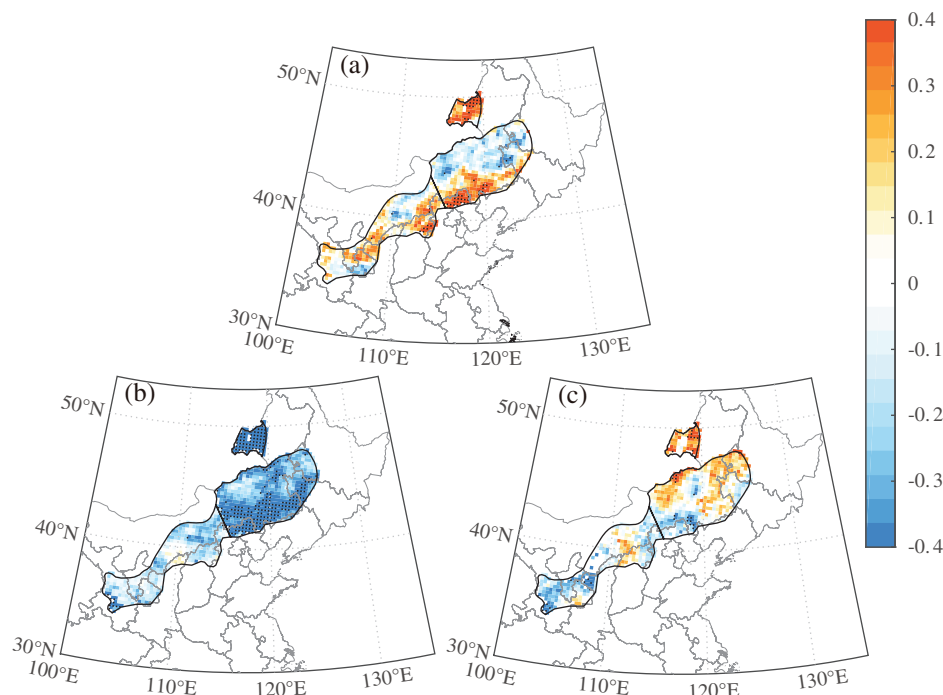


FIGURE 8 Same with Figure 6, but for each component of surface energy budget and only for summer, that is, June–August

3.4 | Effects of vegetation dynamics on the surface energy budget

The above results show that the climatic effects of vegetation growth are the most prominent in summer among the three seasons. Therefore, the following analysis focuses on summer. The modulation of the surface energy budget is a key way by which vegetation affects the local climate. Figure 8 shows significant correlations between the ΔLAI and departures of surface-reflected shortwave radiation (R_{\uparrow}), sensible

heat flux (H), latent heat flux (λE), and ground heat flux (G) in the DYN simulations referring to FIX simulations. There is a negative correlation between ΔLAI and ΔR_{\uparrow} ($r = -0.42$, $p < .01$). The decreased R_{\uparrow} with the increased LAI may be explained by the smaller surface albedo resulted from better vegetation growth (Table S2). The better vegetation growth would lead to less R_{\uparrow} and, hence, the more solar radiation is kept on the surface.

The ΔLAI is also negatively correlated with ΔH ($r = -0.57$, $p < .01$) but is positively correlated with λE

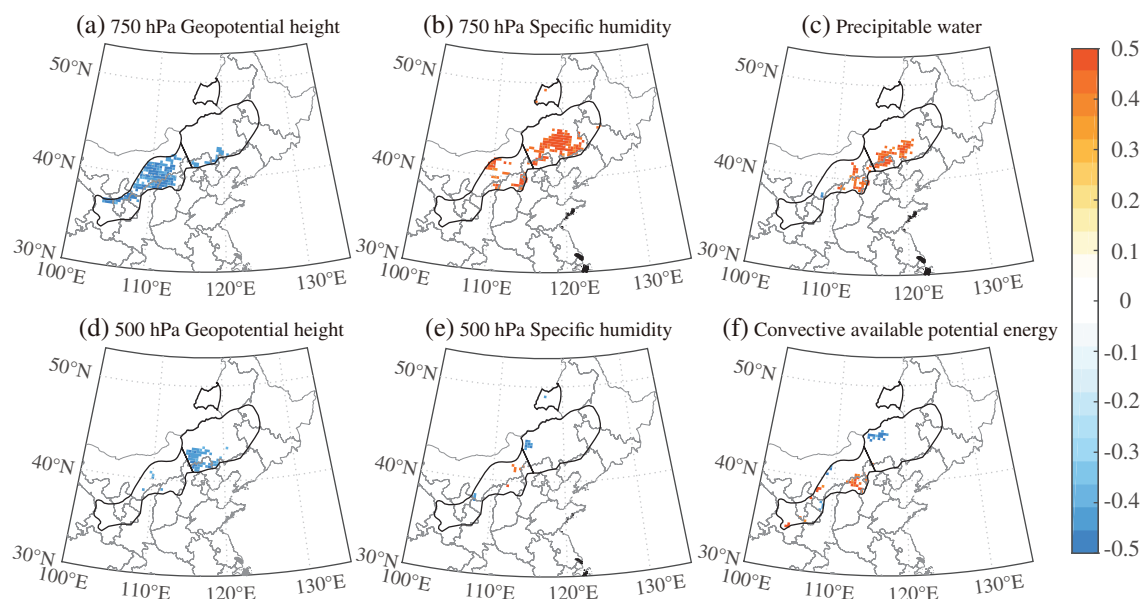


FIGURE 9 Correlation coefficient between ΔLAI and Δ values of local geopotential height, specific humidity, precipitable water, and convective available potential energy in rainy days in the DYN experiment referring to FIX experiment (only the grid with $p \leq .05$ is shown)

($r = .81$, $p < .01$). A higher LAI implies more stomata and, hence, is favourable for transpiration. Moreover, following the abovementioned results (Table 1), a higher LAI generally exists in the context of moist ambient conditions characterized by more precipitation and high soil moisture. It is thereby favourable for soil evaporation as well as stoma resistance decrease, as a result, strengthens transpiration. The higher LAI would therefore be accompanied by stronger evapotranspiration. The positive correlation between the ΔLAI and λE is hence reasonable. A higher LAI may potentially darken the surface and lead to more surface net radiation, which is however much less than an intensified λE (Figure 8); moreover, the ΔG is very weakly. As a consequence, to maintain the surface energy balance, the strengthened λE would usually be accompanied by decreased H . Therefore, there is a negative correlation between the ΔLAI and ΔH . Because H is the energy that directly heats the near-surface air, a declined H in accompany with a high LAI explains the abovementioned cooling effect of vegetation growth.

Moreover, a positive correlation ($r = .43$, $p < .01$) also exists between the ΔLAI and ΔG . Such correlation suggests that G increases with the vegetation growth. As mentioned above, a high LAI generally exists in the context of moist ambient conditions and more soil moisture. Moist soil would be more favourable for thermal conduction than dry soil. The positive correlation for G is thereby explained.

3.5 | Effects on atmospheric thermodynamics

Rainfall is determined together by abundant water vapour, air lifting and condensation, and growth of cloud droplets. To understand the modifications of vegetation growth on summer precipitation, this study analyses the correlations between the ΔLAI and departures of local meteorological factors in DYN experiments referring to FIX experiments. These factors include air specific humidity, precipitable water, column-integrated water vapour flux divergence, vertical velocity, geopotential height, vorticity, planet boundary layer height, and convective available potential energy (CAPE). Significant correlations exist only for the geopotential height, air specific humidity, and precipitable water (Figure 9).

Figure 9 shows that accompanying a high LAI, there would be high specific humidity and precipitable water as well as low geopotential height. High specific humidity and precipitable water mainly exist at a pressure level of 750 hPa, indicating a lower level of air, while there is no detectable increase in specific humidity at 500 hPa. Significantly higher specific humidity and precipitable water mainly occur over the southeastern partition of the study area, where more precipitation occurs. The lower geopotential height also mainly occurs at the pressure level of 750 hPa, while it is very weak at the pressure level of 500 hPa. The lower geopotential height at the pressure level of 750 hPa mainly occurs in the southwestern subregion rather than the southeastern partition where more precipitation occurs.

Therefore, more precipitation over the southeastern partition may be explained by higher specific humidity and precipitable water. The vegetation growth, that is, increased LAI may intensify evapotranspiration and hence supply more water vapour to the atmosphere, which is favourable for precipitation; in return, more precipitation may further promote vegetation growth and more evapotranspiration. Ultimately, a positive feedback loop for the local water cycle manifests itself.

4 | DISCUSSIONS

On behalf of the regional mean shown in Figures 6 and 8, the cooling and precipitation effects of vegetation growth were detected. Moreover, we also found that these effects, particularly precipitation effects, mainly occurred in the central-south partition rather than the entire study area (Figure 7a). The central-south partition of the study area has abundant vegetation–climate interactions. The potential reason may be related to the geographic environment. This area is the connection between the Inner Mongolia Plateau in the north and the North China Plain in the south. The topography is complex and favourable for turbulence and convection. As a result, surface heat and moisture flux changes due to vegetation growth status anomalies easily modulate convection rainfall. Additionally, due to the effects of the East Asia summer monsoon, the precipitable water decreases from southeast to northwest. In the study area, there is more precipitable water at the southeast edge and less water at the northwest edge. As a result, the atmospheric turbulence and convection caused by surface heat and moisture flux changes at the southeast edge may easily lead to modulated rainfall.

As reviewed in the introduction, many existing studies have reported that vegetation category conversions can exert significant effects on the local climate (Xue, 1996; Yu *et al.*, 2013; Cao *et al.*, 2019; Ge *et al.*, 2020). This study shows that even if vegetation category keeps unchanged, climate variability-induced vegetation dynamics can also exert significant effects on the local climate. This study also highlights the importance of evapotranspiration on local precipitation, which is consistent with existing studies. However, this study did not detect effects on precipitation over remote areas, which were reported by existing studies (e.g., Yu *et al.*, 2013). One of the main reasons may be that this study uses only the LAI, GVF, and ALB to parameterize vegetation dynamics rather than includes canopy height regulating the surface roughness and Z_0 . Due to missing dynamic canopy heights, the wind speed and turbulence are barely impacted by vegetation dynamics, and the remote effects may therefore be too slight to be detected. The another reason may be that climate

variability-induced LAI, GVF, and ALB changes with fixed vegetation category are much smaller than those changes induced by vegetation category conversions. As shown in Figure 2, the maximum range of LAI variations at the interannual scale is approximately $0.6 \text{ m}^2 \cdot \text{m}^{-2}$, which existed in July for the northeastern subregion, whereas the discrepancies among grassland, cropland, and woodland were much larger than $1 \text{ m}^2 \cdot \text{m}^{-2}$ under the default WRF-Noah model. Additionally, the climate variability-induced LAI, GVF, and ALB changes could only be predicted in part rather than fully (Tables S1 and S2). The surface radiation and energy budget changes modulated by vegetation dynamics may be much smaller than those modulated by vegetation category conversions. The sufficiently large surface radiation and energy budget changes due to vegetation category conversions may lead to circulation regulations and, hence, remote effects, whereas these changes predicted by VED scheme may not be strong enough to exert effects on remote areas.

It is also noted the VED scheme is generally expected to improve the performance of WRF model, because it provides a dynamic vegetation canopy which is more closer to reality than the default fixed vegetation canopy. However, it is hard to detect the improvements. The reasons are complex. Firstly, the underlying mechanisms of precipitation remain unclear so far and the parameterizations, such as microphysical parameterization and cumulus convection parameterization, have yet large uncertainties. These physics-based models could present the interactions among the components of regional climate and, thereby, are used to examine the role of VED on regional climate. However, the large number of parameters embed into these parameterizations are experiences-based. These parameters are mostly derived from measurements over other area and may be mismatching with the study area. So, it is hard to improve performances of WRF only through implementing a local experiences-based VED scheme. Second, as mentioned above, the VED scheme predicts only part of variations of LAI (Table 1). Figures 6 and 8 show significant linear correlation between ΔLAI and ΔT , ΔP . Thereby, under the condition of underestimated ΔLAI , the feedback intensity of VED on local temperature and precipitation would be also underestimated. Thereby, contributions of local experiences-based VED scheme would be not strong enough to be detected.

Finally, under the WRF model frame, the Noah land surface model (LSM) with mutiparameterization options (Noah-MP) is actually built by incorporating improved physics and multiple options of land surface processes parameterization schemes, which includes dynamic vegetation module (Niu *et al.*, 2011). This dynamic vegetation module consists of plant photosynthesis submodel, respiration submodel, carbon allocation submodel, and so on. In comparison to our

VED scheme, the dynamic vegetation module in the Noah-MP is more complex and more perfect theoretically. However, the evaluations reported that simulated LAI and GVF from Noah-MP have large bias. For instance, Li *et al.* (2022) reported that it produced bias in annual mean LAI and gross primary production (GPP) by more than 40% in most herbaceous regions over the world. Ma *et al.* (2017) reported that it produced bias in annual mean GPP and evapotranspiration (ET) by more than 30% and 20%, respectively, while produced bias in sensible heat flux by less than 20% in semiarid area in central-western Continental United States. These biases from offline simulations suggest that the Noah-MP model with dynamic vegetation module has intrinsic uncertainties. These uncertainties are derived from errors in model structure and parameters (Li *et al.*, 2020). In case of activating it in the WRF modelling, since the atmospheric component also have large uncertainties, the coupled WRF modelling would have much larger uncertainties. The feedback of vegetation dynamics may be concealed by so large uncertainties and, hence, hard to be detected. This study used the empirical VED models keeping observed normal mean of LAI, GVF, and ALB; as a consequence, uncertainties of WRF modelling was in control. The effects of vegetation dynamic could be detected from WRF modelling. This is the main reason why this study built empirical VED models rather than use Noah-MP model with dynamic vegetation module.

5 | SUMMARY

This belt-like study area is located on the northwest margin of the EASM and dominated by a semiarid climate. Due to the potential water deficit in the semiarid environment, the summer vegetation growth status sensitively responds to precipitation anomalies caused by strong EASM anomalies. Following the linear regression model, the precipitation in the previous month may explain slightly more than half of the total variance in the warm-season LAI at the interannual scale. In the context of stronger EASM years, there would be more summer precipitation and, hence, better vegetation growth. There would be a higher LAI and GVF as well as a lower ALB. As a response, surface-reflected solar radiation decreases, whereas surface-captured solar radiation increases; moreover, more net surface radiation is mainly released through evapotranspiration, that is, as latent heat, while sensible heat decreases. As a consequence, the local climate would experience cooling; atmospheric precipitable water increases due to increased evapotranspiration and, hence, leads to more precipitation.

This study suggests that a positive “precipitation–vegetation–precipitation” feedback loop exists in the SA area. Such a positive feedback loop have also been reported for the Amazon area covered by rainforest (Wang *et al.*, 2011) and the Sahel area covered by tropical grassland (Zeng *et al.*, 1999). This study pays attention to the SA area in north China, which is dominantly covered by temperate grassland. Taking together with existing studies, we conclude that detectable modulations of vegetation dynamics on climate exist not only in tropical areas but also in temperate areas. Moreover, all these studies highlight modulations of vegetation dynamics on interannual and interdecadal climate variability rather than on the long-term trend of climate changes associated with anthropogenic GHG emissions. All these studies implicate a climate-vegetation feedback loop that would enlarge precipitation variability. Hence, to explicitly predict climate variations, it is worth developing explicit climate-vegetation interaction schemes and implementing them in coupled climate models, such as the WRF-Noah model.

AUTHOR CONTRIBUTIONS

Xuezhen Zhang designed the entire research, interpreted the analysis results, and prepared the manuscript. Xinrui Liu visualized the results, performed the analysis, and contributed the manuscript. Jiazhe Chen conducted the experiment and performed the analysis. Qihong Tang and Yilong Wang provided constructive comments and improved the manuscript.

ACKNOWLEDGEMENTS

This research is supported by the National Natural Science Foundation of China (No. 41790424) and the National Key Research and Development Program of China (No. 2019YFA0606600).

DATA AVAILABILITY STATEMENT

All of the data used in this study are publicly available. The data used to evaluate the WRF modelling are provided by the National Meteorology Science Data Center of China (<http://data.cma.cn>). Lateral boundary forcing and sea surface temperature (SST) data are derived from the NCEP II reanalysis dataset, which is available from the RDA (<http://dss.ucar.edu>). The ERA5 dataset is provided by the European Centre for Medium-Range Weather Forecasts (ECMWF) and can be accessed from <https://www.ecmwf.int/en/forecasts/datasets/reanalysis-datasets/era5>. The land surface parameter dataset is provided by the National Aeronautics and Space Administration (NASA) at <https://modis.gsfc.nasa.gov/>. The output data of WRF simulations in this study are too large to share via the public domain. The data and codes of this study are available from the corresponding author by request.

ORCID

Xuezhen Zhang  <https://orcid.org/0000-0002-3845-2403>

QiuHong Tang  <https://orcid.org/0000-0002-0886-6699>

REFERENCES

- Bai, M., Zheng, J., Hao, Z., Zhang, X. and Zeng, G. (2019) Hydroclimate patterns over the Northern Hemisphere when megadroughts occurred in north China during the last millennium. *Climatic Change*, 157, 365–385. <https://doi.org/10.1007/s10584-019-02580-w>.
- Bonan, G.B. (2008) Forests and climate change: forcings, feedbacks, and the climate benefits of forests. *Science*, 320(5882), 1444–1449. <https://doi.org/10.1126/science.1155121>.
- Cao, Q., Wu, J., Yu, D. and Wang, W. (2019) The biophysical effects of the vegetation restoration program on regional climate metrics in the Loess Plateau, China. *Agricultural and Forest Meteorology*, 268, 169–180. <https://doi.org/10.1016/j.agrformet.2019.01.022>.
- Chen, F. and Dudhia, J. (2001) Coupling an advanced land surface-hydrology model with the Penn State-NCAR MM5 modeling system. Part I: model implementation and sensitivity. *Monthly Weather Review*, 129, 569–585. [https://doi.org/10.1175/1520-0493\(2001\)129<0569:CAALSH>2.0.CO;2](https://doi.org/10.1175/1520-0493(2001)129<0569:CAALSH>2.0.CO;2).
- Chen, J., Huang, W., Feng, S., Zhang, Q., Kuang, X., Chen, J. and Chen, F. (2021) The modulation of westerlies-monsoon interaction on climate over the monsoon boundary zone in East Asia. *International Journal of Climatology*, 41, E3049–E3064. <https://doi.org/10.1002/joc.6903>.
- Chen, J., Huang, W., Jin, L.Y., Chen, J.H., Chen, S.Q. and Chen, F. H. (2018) A climatological northern boundary index for the east Asian summer monsoon and its interannual variability. *Science China Earth Sciences*, 61, 13–22. <https://doi.org/10.1007/s11430-017-9122-x>.
- Chen, K., Ning, L., Liu, Z., Liu, J., Yan, M., Sun, W., Yuan, L., Lv, G., Li, L., Jin, C. and Shi, Z. (2020) One drought and one volcanic eruption influenced the history of China: the late Ming Dynasty Mega-drought. *Geophysical Research Letters*, 47, e2020GL088124. <https://doi.org/10.1029/2020GL088124>.
- Chen, Y.Y., Yang, K., Zhou, D.G., Qin, J. and Guo, X.F. (2010) Improving the Noah Land Surface Model in arid regions with an appropriate parameterization of the thermal roughness length. *Journal of Hydrometeorology*, 11, 995–1006. <https://doi.org/10.1175/2010JHM1185.1>.
- Collins, W.D., Rasch, P.J., Boville, B.A., Hack, J.J., McCaa, J.R., Williamson, D.L., Kiehl, J.T. and Briegleb, B. (2004) *Description of the NCAR community atmosphere model (CAM 3.0)*. Boulder, CO: NCAR. Technical note: NCAR/TN-464+ STR, pp. 1326–1334.
- Cui, Y. (2013) Preliminary estimation of the realistic optimum temperature for vegetation growth in China. *Environmental Management*, 52, 151–162. <https://doi.org/10.1007/s00267-013-0065-1>.
- Dai, L., Wright, J.S. and Fu, R. (2020) Moisture and energy budget perspectives on summer drought in north China. *Journal of Climate*, 33, 10149–10167. <https://doi.org/10.1175/JCLI-D-20-0176.1>.
- Ding, Y., Xu, J., Wang, X., Peng, X. and Cai, H. (2020) Spatial and temporal effects of drought on Chinese vegetation under different coverage levels. *Science of the Total Environment*, 716, 137166. <https://doi.org/10.1016/j.scitotenv.2020.137166>.
- Ding, Y.H. and Chan, J.C.L. (2005) The East Asian summer monsoon: an overview. *Meteorology and Atmospheric Physics*, 89, 117–142. <https://doi.org/10.1007/s00703-005-0125-z>.
- Feng, J., Wang, L. and Chen, W. (2014) How does the East Asian summer monsoon behave in the decaying phase of El nino during different PDO phases? *Journal of Climate*, 27(7), 2682–2698. <https://doi.org/10.1175/JCLI-D-13-00015.1>.
- Forzieri, G., Miralles, D.G., Ciais, P., Alkama, R., Ryu, Y., Duveiller, G., Zhang, K., Robertson, E., Kautz, M., Martens, B., Jiang, C., Arneth, A., Georgievski, G., Li, W., Ceccherini, G., Anthoni, P., Lawrence, P., Wiltshire, A., Pongratz, J., Piao, S., Sitch, S., Goll, D.S., Arora, V.K., Lienert, S., Lombardozzi, D., Kato, E., Nabel, J.E.M.S., Tian, H., Friedlingstein, P. and Cescatti, A. (2020) Increased control of vegetation on global terrestrial energy fluxes. *Nature Climate Change*, 10, 356–362. <https://doi.org/10.1038/s41558-020-0717-0>.
- Ge, J., Pitman, A., Guo, W., Zan, B. and Fu, C. (2020) Impact of revegetation of the loess plateau of China on the regional growing season water balance. *Hydrology and Earth System Sciences*, 24, 515–533. <https://doi.org/10.5194/hess-24-515-2020>.
- Ge, Q., Zhang, X. and Zheng, J. (2014) Simulated effects of vegetation increase/decrease on temperature changes from 1982 to 2000 across the eastern China. *International Journal of Climatology*, 34(1), 187–196. <https://doi.org/10.1002/joc.3677>.
- Gong, D.Y., Shi, P.J. and Wang, J.A. (2004) Daily precipitation changes in the semi-arid region over northern China. *Journal of Arid Environments*, 59(4), 771–784. <https://doi.org/10.1016/j.jaridenv.2004.02.006>.
- Grell, G.A. and Dévényi, D. (2002) A generalized approach to parameterizing convection combining ensemble and data assimilation techniques. *Geophysical Research Letters*, 29, 38-1–38-4. <https://doi.org/10.1029/2002GL015311>.
- Han, Y., Peng, J., Meersmans, J., Liu, Y., Zhao, Z. and Mao, Q. (2018) Integrating spatial continuous wavelet transform and normalized difference vegetation index to map the agro-pastoral transitional zone in northern China. *Remote Sensing*, 10(12), 1928. <https://doi.org/10.3390/rs10121928>.
- Hao, R. and Yu, D. (2018) Optimization schemes for grassland ecosystem services under climate change. *Ecological Indicators*, 85, 1158–1169. <https://doi.org/10.1016/j.ecolind.2017.12.012>.
- Hersbach, H., Bell, B., Berrisford, P., Hirahara, S., Horányi, A., Muñoz-Sabater, J., Nicolas, J., Peubey, C., Radu, R., Schepers, D., Simmons, A., Soci, C., Abdalla, S., Abellan, X., Balsamo, G., Bechtold, P., Biavati, G., Bidlot, J., Bonavita, M., Chiara, G.D., Dahlgren, P., Dee, D., Diamantakis, M., Dragani, R., Flemming, J., Forbes, R., Fuentes, M., Geer, A., Haimberger, L., Healy, S., Hogan, R.J., Hólm, E., Janisková, M., Keeley, S., Laloyaux, P., Lopez, P., Lupu, C., Radnoti, G., Rosnay, P.D., Rozum, I., Vamborg, F., Villaume, S. and Thépaut, J. (2020) The ERA5 global reanalysis. *Quarterly Journal of the Royal Meteorological Society*, 146, 1999–2049. <https://doi.org/10.1002/qj.3803>.
- Hong, S.Y., Dudhia, J. and Chen, S.H. (2004) A revised approach to ice microphysical processes for the bulk parameterization of clouds and precipitation. *Monthly Weather Review*, 132, 103–120. [https://doi.org/10.1175/1520-0493\(2004\)132<0103:ARATIM>2.0.CO;2](https://doi.org/10.1175/1520-0493(2004)132<0103:ARATIM>2.0.CO;2).
- Hong, S.Y. and Pan, H.L. (1996) Nonlocal boundary layer vertical diffusion in a medium-range forecast model. *Monthly Weather Review*, 124, 2322–2339.
- Huang, J., Li, Y., Fu, C., Chen, F., Fu, Q., Dai, A., Shinoda, M., Ma, Z., Guo, W., Li, Z., Zhang, L., Liu, Y., Yu, H., He, Y., Xie, Y., Guan, X., Ji, M., Lin, L., Wang, S., Yan, H. and Wang, G. (2017)

- Dryland climate change: recent progress and challenges. *Reviews of Geophysics*, 55, 719–778. <https://doi.org/10.1002/2016RG000550>.
- Jiang, H., Xu, X., Guan, M., Wang, L., Huang, Y. and Jiang, Y. (2020) Determining the contributions of climate change and human activities to vegetation dynamics in agro-pastoral transitional zone of northern China from 2000 to 2015. *Science of the Total Environment*, 718, 134871. <https://doi.org/10.1016/j.scitotenv.2019.134871>.
- Karnieli, A., Ohana-Levi, N., Silver, M., Paz-Kagan, T., Panov, N., Varghese, D., Chrysoulakis, N. and Provenzale, A. (2019) Spatial and seasonal patterns in vegetation growth-limiting factors over Europe. *Remote Sensing*, 11(20), 2406. <https://doi.org/10.3390/rs11202406>.
- Li, J., Chen, F., Lu, X., Gong, W., Zhang, G. and Gan, Y. (2020) Quantifying contributions of uncertainties in physical parameterization schemes and model parameters to overall errors in Noah-MP dynamic vegetation modeling. *Journal of Advances in Modeling Earth Systems*, 12, e2019MS001914. <https://doi.org/10.1029/2019MS001914>.
- Li, J., Miao, C., Zhang, G., Fang, Y.-H., Shangguan, W. and Niu, G.-Y. (2022) Global evaluation of the Noah-MP land surface model and suggestions for selecting parameterization schemes. *Journal of Geophysical Research: Atmospheres*, 127, e2021JD035753. <https://doi.org/10.1029/2021JD035753>.
- Liu, J.H., Gao, J.X., Lv, S.H., Han, Y.W. and Nie, Y.H. (2011) Shifting farming-pastoral ecotone in China under climate and land use changes. *Journal of Arid Environments*, 75(3), 298–308. <https://doi.org/10.1016/j.jaridenv.2010.10.010>.
- Ma, N., Niu, G.-Y., Xia, Y., Cai, X., Zhang, Y., Ma, Y. and Fang, Y. (2017) A systematic evaluation of Noah-MP in simulating land-atmosphere energy, water, and carbon exchanges over the continental United States. *Journal of Geophysical Research: Atmospheres*, 122(22), 12245–12268. <https://doi.org/10.1002/2017jd027597>.
- Niu, G.-Y., Yang, Z.-L., Mitchell, K.E., Chen, F., Ek, M.B., Barlage, M., Kumar, A., Manning, K., Niyogi, D., Rosero, E., Tewari, M. and Xia, Y. (2011) The community Noah land surface model with multiparameterization options (Noah-MP): 1. Model description and evaluation with local-scale measurements. *Journal of Geophysical Research*, 116, D12109. <https://doi.org/10.1029/2010JD015139>.
- Purevjav, G. and Luvsan, N. (2004) *The impact of desertification on Mongolian climate and its numerical study using regional climate model (RegCM3)*. Paper presented at Proceedings of the 3rd International Workshop on Terrestrial Change in Mongolia/2 Joint Workshop of AMPEX, IORGC and RAISE Projects. TERC, University of Tsukuba.
- Santanello, J.A., Jr., Dirmeyer, P.A., Ferguson, C.R., Findell, K.L., Tawfik, A.B., Berg, A., Ek, M., Gentile, P., Guillod, B.P., Heerwaarden, C.V., Roundy, J. and Wulfmeyer, V. (2018) Land-atmosphere interactions: the LoCo perspective. *Bulletin of the American Meteorological Society*, 99, 1253–1272. <https://doi.org/10.1175/BAMS-D-17-0001.1>.
- Skamarock, W.C., Klemp, J.B. and Dudhia, J. (2008) *A description of the advanced research WRF model version 4*. Boulder, CO: NCAR, 145 pp.
- Song, L., Jin, J. and He, J. (2019) Effects of severe water stress on maize growth processes in the field. *Sustainability*, 11, 5086. <https://doi.org/10.3390/su11185086>.
- Wang, G., Huang, J., Guo, W., Zuo, J., Wang, J., Bi, J., Huang, Z. and Shi, J. (2010) Observation analysis of land-atmosphere interactions over the Loess Plateau of northwest China. *Journal of Geophysical Research*, 115, D00K17. <https://doi.org/10.1029/2009JD013372>.
- Wang, G., Sun, S. and Mei, R. (2011) Vegetation dynamics contributes to the multi-decadal variability of precipitation in the Amazon region. *Geophysical Research Letters*, 38, L19703. <https://doi.org/10.1029/2011GL049017>.
- Wi, L., Zhang, J. and Dong, W. (2011) Vegetation effects on mean daily maximum and minimum surface air temperatures over China. *Chinese Science Bulletin*, 56(9), 900–905. <https://doi.org/10.1007/s11434-011-4349-7>.
- Xu, Y., Gao, X.-J., Shen, Y., Xu, C.H., Shi, Y. and Giorgi, F. (2009) A daily temperature dataset over China and its application in validating a RCM simulation. *Advances in Atmospheric Sciences*, 26, 763–772. <https://doi.org/10.1007/s00376-009-9029-z>.
- Xue, Y. (1996) The impact of desertification in the Mongolian and the Inner Mongolian grassland on the regional climate. *Journal of Climate*, 9(9), 2173–2189. [https://doi.org/10.1175/1520-0442\(1996\)009<2173:TIODIT>2.0.CO;2](https://doi.org/10.1175/1520-0442(1996)009<2173:TIODIT>2.0.CO;2).
- Yang, K., Koike, T., Ishikawa, H., Kim, J., Li, X., Liu, H., Liu, S., Ma, Y. and Wang, J. (2008) Turbulent flux transfer over bare-soil surfaces: characteristics and parameterization. *Journal of Applied Meteorology and Climatology*, 47(1), 276–290. <https://doi.org/10.1175/2007JAMC1547.1>.
- Yu, E., Wang, H., Sun, J. and Gao, Y. (2013) Climatic response to changes in vegetation in the Northwest Hetao Plain as simulated by the WRF model. *International Journal of Climatology*, 33(6), 1470–1481. <https://doi.org/10.1002/joc.3527>.
- Yu, L. (2016) Agro-pastoralism under climate change: institutions and local climate adaptations in northern China. *Land Use Policy*, 58, 173–182. <https://doi.org/10.1016/j.landusepol.2016.07.022>.
- Zeng, N., Neelin, J.D., Lau, K.M. and Tucker, C.J. (1999) Enhancement of Interdecadal climate variability in the Sahel by vegetation interaction. *Science*, 286, 1537–1540. <https://doi.org/10.1126/science.286.5444.1537>.
- Zhang, J., Dong, W. and Fu, C. (2005) Impact of land surface degradation in northern China and southern Mongolia on regional climate. *Chinese Science Bulletin*, 50, 75–81. <https://doi.org/10.1360/04wd0054>.
- Zhang, Q., Wang, S. and Wei, G. (2003) A study on physical parameters of local land-surface processes on the Gobi in northeast China. *Chinese Journal of Geophysics*, 46(5), 883–895. <https://doi.org/10.1002/cjg2.408>.
- Zhang, X., Wu, M., Liu, Y., Hao, Z. and Zheng, J. (2018) The relationship between the East Asian summer monsoon and El Niño–Southern Oscillation revealed by reconstructions and a control simulation for millennium. *Quaternary International*, 493, 106–113. <https://doi.org/10.1016/j.quaint.2018.06.024>.
- Zhang, X., Zhang, Z. and Song, S. (2021) Modulation of vegetation restoration on outdoor thermal comfort over the Loess Plateau, China from 1982 to 2015. *Environmental Research Communications*, 3(1), 015002.
- Zhang, Y., Kendy, E., Qiang, Y., Liu, C., Shen, Y. and Sun, H. (2004) Effect of soil water deficit on evapotranspiration, crop

- yield, and water use efficiency in the North China Plain. *Agricultural Water Management*, 64(2), 107–122.
- Zheng, J.Y., Bian, J.J., Ge, Q.S., Hao, Z.X., Yin, Y.H. and Liao, Y.M. (2013) The climate regionalization in China for 1981–2010. *Chinese Science Bulletin*, 58, 3088–3099 (in Chinese). <https://doi.org/10.1360/972012-1491>.
- Zheng, Z., Wei, Z., Li, Z., Wei, H. and Liu, H. (2014) Study of parameterization of surface albedo of bare soil over the Gobi desert in the Dunhuang region. *Chinese Journal of Atmospheric Sciences*, 38(2), 297–308 (in Chinese). <https://doi.org/10.3878/j.issn.1006-9895.2013.13147>.
- Zheng, Z., Wei, Z., Wen, Z., Dong, W., Li, Z., Wen, X., Zhu, X., Ji, D., Chen, C. and Yan, D. (2017) Inclusion of solar elevation angle in land surface albedo parameterization over bare soil surface. *Journal of Advances in Modeling Earth Systems*, 9(8), 3069–3081. <https://doi.org/10.1002/2017MS001109>.

SUPPORTING INFORMATION

Additional supporting information can be found online in the Supporting Information section at the end of this article.

How to cite this article: Zhang, X., Liu, X., Chen, J., Tang, Q., & Wang, Y. (2023). Responses and feedbacks of vegetation dynamics to precipitation anomaly over the semiarid area of north China: Evidences from simulations of the WRF-Noah model. *International Journal of Climatology*, 43(2), 804–817. <https://doi.org/10.1002/joc.7830>